Design and Control of a Bio-Inspired Human-Friendly Robot

Dongjun Shin*, Irene Sardellitti†, Yong-Lae Park‡, Oussama Khatib*, and Mark Cutkosky‡

Abstract

The increasing demand for physical interaction between humans and robots has led to an interest in robots that guarantee safe behavior when human contact occurs. However, attaining established levels of performance while ensuring safety creates formidable challenges in mechanical design, actuation, sensing and control. To promote safety without compromising performance, a human-friendly robotic arm has been developed using the concept of hybrid actuation. The new design employs high power, low impedance pneumatic artificial muscles augmented with small electrical actuators, distributed compact pressure regulators with proportional valves, and hollow plastic links. The experimental results show that significant performance improvement can be achieved with hybrid actuation over a system with pneumatic muscles alone. The paper evaluates the safety of the new robot arm through experiments and simulation, demonstrating that its inertia/power characteristics surpass those of previous human-friendly robots we have developed.

1 Introduction

There is a growing interest in applications involving close physical interaction between robots and humans in such areas as medicine, home care, manufacturing and entertainment. A major challenge in such applications is safety: How can robots be sufficiently fast, strong, and accurate to do useful work while also being inherently safe for physical interaction?

Traditionally, safety in human-robot interaction was guaranteed on the basis of prevention of collisions. For the past decade, considerable work has been done on real time obstacle avoidance [Khatib (1986)]. Several sensing strategies have been proposed such as compliant and energy-absorbing layers with proximity sensors [Novak and Feddema (1992)], sensitive skin [Lumelsky and Cheung (1993)], and camera systems [Ebert and Henrich (2002)] in order to detect impending collisions. Strategies for detecting the collision while quickly reacting in a safe manner have

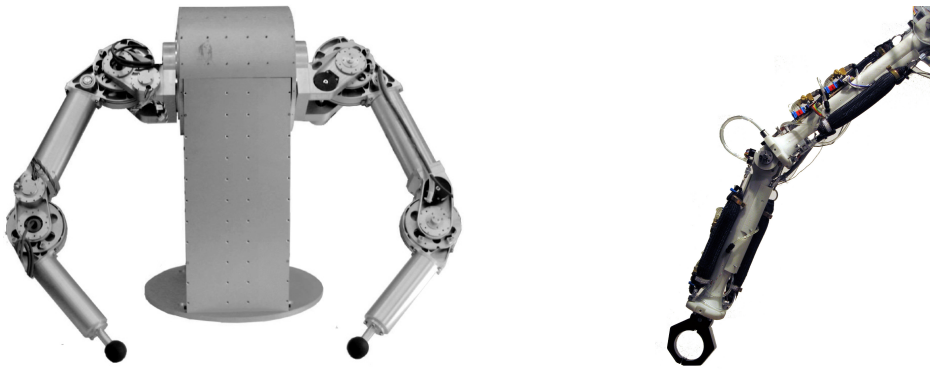

(a) 3DOF Human Friendly Robot (b) $S2\rho$ 1.0

Figure 1: (a) Distributed Macro-Mini Actuation, DM^2, design achieves a significant increase in the control bandwidth and reduction in the effective inertia when compared with traditional actuation schemes [Zinn et al. (2004)]. (b) Stanford Safety Robot, $S2\rho$, provides light yet powerful actuation and reduces complexity of design and manufacturing [Shin et al. (2008)].

*Artificial Intelligence Laboratory, Stanford University, Stanford, CA 94305, USA. {djshin, ok}@robotics.stanford.edu

†Advanced Robotics Laboratory, Italian Institute of Technology, Genoa, Italy. irene.sardellitti@iit.it

‡Department of Mechanical Engineering, Stanford University, Stanford, CA 94305, USA. {ylpark, cutkosky}@stanford.edu

also been developed [De Luca et al. (2006); Haddadin et al. (2008)]. Although these approaches play a significant role in enhancing the safety in physical human-robot interaction, it remains desirable to minimize the inertia of the robot while maintaining sufficient power and precision for everyday tasks.

To develop a light, strong and accurate robot however, is not straightforward since robots have traditionally relied on electromagnetic actuators, which offer excellent controllability but poor power-to-weight ratio. Previous efforts to increase the safety of robot arms while maintaining control performance have included relocating the actuators to the base and powering the joints with cables [Salisbury et al. (1989)] and employing a series elastic actuator [Pratt and Williamson (1995)]. Other work has employed variable stiffness for both performance and safety [English and Russell (1999); Bicchi and Tonietti (2004); Migliore et al. (2005); Schiavi et al. (2008)]. Approaches based on artificial pneumatic muscles alone have also been proposed [Tonietti and Bicchi (2002)]. Other strategies that adopt two actuators for each degree-of-freedom have included employing parallel-coupled macro and micro actuators [Morrel (1996)] and controlling the stiffness and joint position with an individual actuator for each respective property [Van Ham et al. (2007); Wolf and Hirzinger (2008)]. A summary of current challenges and technologies for human-safe robotics is provided in [Bicchi et al. (2008)].

At the same time, several researchers have introduced criteria in order to quantify and evaluate the safety of their robotic arms. Zinn has proposed the Manipulator Safety Index (MIS) attempting in evaluating the safety in terms of effective inertia, impact velocity, and interface stiffness between human and robot [Zinn (2005)]. Heinzmann has defined the impact potential to describe the ability of a robot to cause impact [Heinzmann and Zelinsky (2003)]. Bicchi evaluates the safety of different joint actuation schemes in terms of the velocity upper limit, which is obtained by the Head injury Criteria (HIC) [Bicchi and Tonietti (2004)]. Haddadin highlights the role of joint velocity in impact injury through extensive crash tests with dummies [Haddadin et al. (2007, 2008)].

1.1 Hybrid Actuation for Human Friendly Robot

Our efforts in developing the human-friendly robot over the past several years at the Stanford AI Lab produced Distributed Macro-Mini (DM^2) actuation, as shown in Fig. 1 (a) [Zinn et al. (2004)], which provides a combination of high power, low impedance, and precise control. Large (macro), low frequency actuators are located at the base of the robot

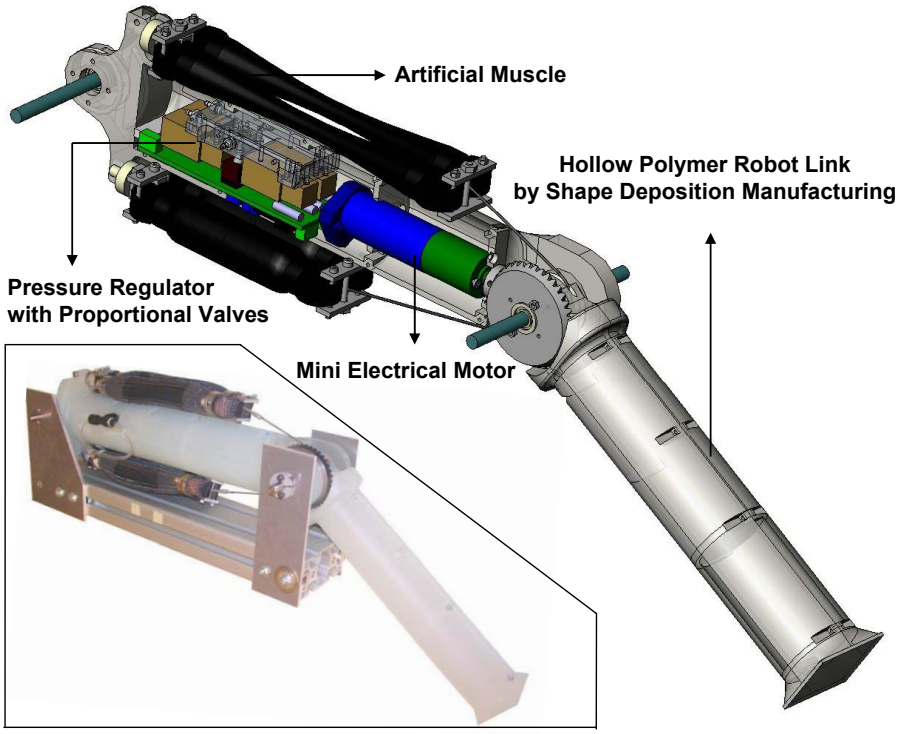

Figure 2: Revised $S2\rho$ (version 1.5) elbow design and single DOF benchtop prototype.

arm as the main source of mechanical power; small (mini) actuators are located at the joints for fast response. A 3DOF platform with the DM^2 actuation achieves a significant increase in the control bandwidth and reduction in the effective inertia [Thaulad (2005)]. However, the electromagnetic actuators still offer low power/weight ratios compared to pneumatic artificial muscles. Even more limiting is their inability to exert large sustained torques without overheating. Consequently, the motors are used with high transmission ratios and cannot match the low mechanical impedance of artificial muscles [Caldwell et al. (1995); Chou and Hannaford (1996); Tondu and Lopez (2000)]. Furthermore, the extensive cable transmissions used arms like the DM^2 increase the complexity of design and assembly.

The Stanford Safety Robot, $S2\rho$, shown in Fig. 1 (b), is an evolution of the DM^2 approach in which compliant pneumatic muscles replace the macro actuators at the base. In this paper we report on a second iteration of the $S2\rho$ design, which uses compact proportional pressure regulators at each joint for better control of the pneumatic muscles. The pressure regulators, electronics and small electromagnetic actuator for each joint are housed within hollow plastic links. The muscles attach to the links and are themselves covered by a compliant, energy absorbing skin. The distributed pressure regulators decrease air flow resistance and line capacitance, and reduce the complexity of the arm by being located adjacent to the actuators. The plastic link is created using a rapid prototyping process and contains provisions for mounting bearings, electronics, etc. to simplify the design and assembly process. Other improvements of the new design include using four pneumatic muscles per joint, instead of two larger ones, for increased responsiveness and range of motion.

The follow sections present the details of the design, fabrication, actuation, and control of the modified $S2\rho$ arm. We present the results of experiments to characterize the behavior of a single "elbow" link in Section 4 and conclusions in Section 5.

2 Design

2.1 Actuation

The original $S2\rho$ robotic arm used a single pair of McKibben artificial muscles as macro actuator. Pairs of muscles were used in an antagonistic configuration, pulling on a cable that wraps around a pulley at the joint. A limitation of McKibben muscles is that they have a modest ($\approx 22\%$) contraction ratio. A smaller pulley can compensate for the limited muscle stroke, but at the cost of reduced joint torque. To overcome this limitation, the modified $S2\rho$ arm (Fig. 2) uses two McKibben muscles in parallel on each side of the pulley to provide sufficient force without excessive bulk and time to fill and exhaust the muscle chambers. Using a 40.6 mm pulley for a maximum torque of 8.128 Nm, the elbow achieves 121.08 degrees of rotation with appropriate pre-tension. Table 1 compares the characteristics of the original (version 1.0) and new (version 1.5) $S2\rho$ arms.

To meet size and weight requirements, the original $S2\rho$ arm employed small, 4.5g on-off solenoid valves (X-Valve, Parker) to actuate the muscles, with one valve for pressurizing and two for exhausting, to compensate for the lower pressure drop and air flow rate of the exhaust [Van Ham et al. (2003)]. However, these valves resulted in a performance

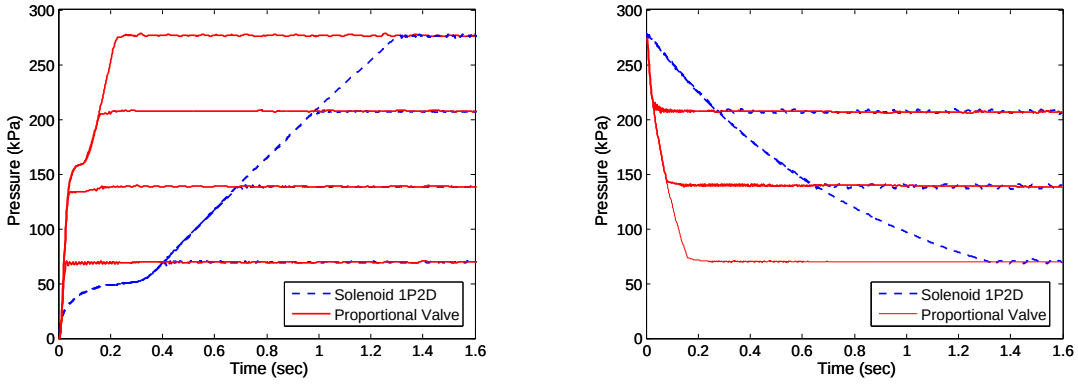

(a) Pressurizing (b) Exhausting

Figure 3: Step response comparison between proportional valves and solenoid valves for pressurizing (a) and exhausting (b) phases. The solenoid valves have one pressurizing valve and two exhausting valves to compensate for asymmetrical behavior due to different pressure drops [Shin et al. (2008)].

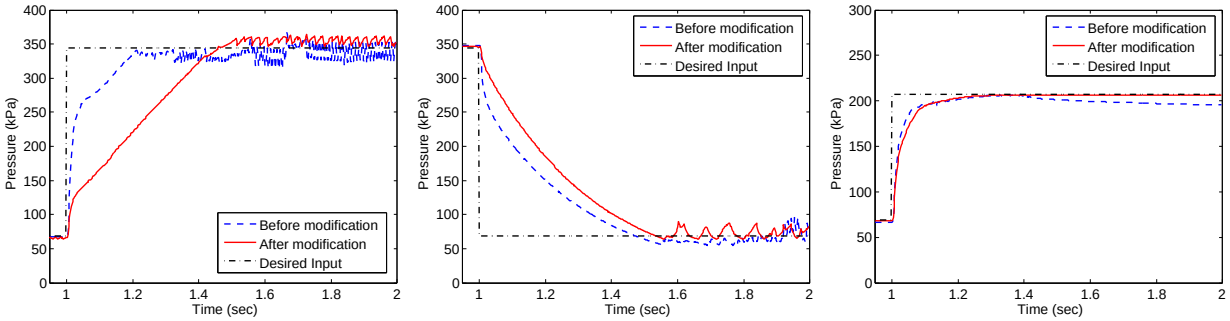

(a) Step Response at Pressurizing (b) Step Response at Exhausting (c) Steady State Error Comparison

Figure 4: Pressure step responses for filling (a) and exhausting (b) show the effect of modifying the manifold so that the measured pressure more accurately reflects muscle pressure, which rises more slowly than pressure at the valve. Before manifold modification, the measured pressure is almost constant instead gradually equalizing between the muscles and manifold-attached sensor when both pressurizing and exhausting valves are closed (c).

	Weight	Max. Torque (Elbow)	Range of Motion (Elbow)
$S2\rho$ 1.0	1.871 kg	4.064 N·m	86.80 °
$S2\rho$ 1.5	1.433 kg	8.128 N·m	121.08 °

Table 1: Testbed Characteristics Comparison

limitation in transient and steady state operation. The restricted flow rate (effective orifice size: 0.51 mm diameter) caused substantial errors in transient response. In addition, their on-off behavior produced undesirable overworking and/or oscillation in steady state operation, especially at high pressure. The new design exploits valves (MD Pro, Parker) with higher flow rates (effective orifice size: 1.27 mm diameter) and a proportional flow control feature. To match the flow rates between pressurizing and exhausting, higher flow rate valves (1.79 mm orifice diameter) are employed for exhausting. As shown in Fig. 3 (a) and (b), the proportional valves achieve a significantly faster initial response and a faster convergence to the desired pressure. (Note that the pressurizing and exhausting phases present an asymmetrical behavior resulting from the different pressure drops across the valves.) The faster response achieved with proportional valves results in the significantly improved joint torque control as discussed in Section 4.

To accommodate the valves, pressure sensors, and driving circuit, a new manifold was designed and fabricated using a version of Shape Deposition Manufacturing (SDM) [Weiss et al. (1997)] that has been adapted for pneumatic bio-inspired robots [Cham et al. (2002)]. As a result of non-collocation of the muscle and valve, there is an inevitable pneumatic delay, which affects response. The effects of back pressure are minimized by increasing the diameter and reducing the length of the air path in the manifold. Figures 4 (a) and (b) show that the measured initial change, which results from the effects of back pressure, is greatly reduced during pressurizing and exhausting. Figure 4 (c) demonstrates that the manifold modification achieves a smaller measured drop in a steady state operation, where both pressurizing and exhausting valves are closed. (Before the manifold modification, the measured pressure between the muscles and the manifold-attached sensor would gradually equalize when all valves were closed.) As a result of these modifications, measurement errors are reduced and the sensor pressure reflects the muscle pressure more accurately.

2.2 Materials and structures

The first-generation $S2\rho$ robotic arm used a porous polymer structure as the central bone-like support with an internal cavity for plumbing the pneumatic connection. The structure was created using selective laser sintering (SLS) with glass-filled nylon. While SLS allowed almost arbitrary shapes to be realized, the resulting parts were not particularly strong for their weight and the tolerances were not adequate for mounting bearings and shafts without post-machining. The new arm is created using SDM, which allows combinations of hard and soft materials, as well as sensors and other discrete parts, to be integrated in a single heterogeneous structure. The new link is a thin-walled shell (Task

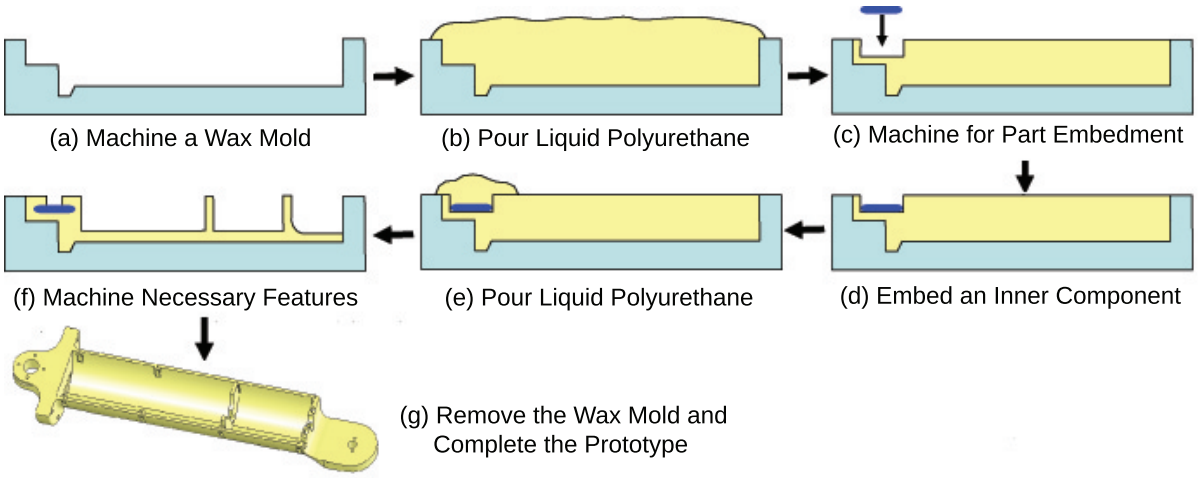

Figure 5: SDM Process for Half Structure of Upper Arm

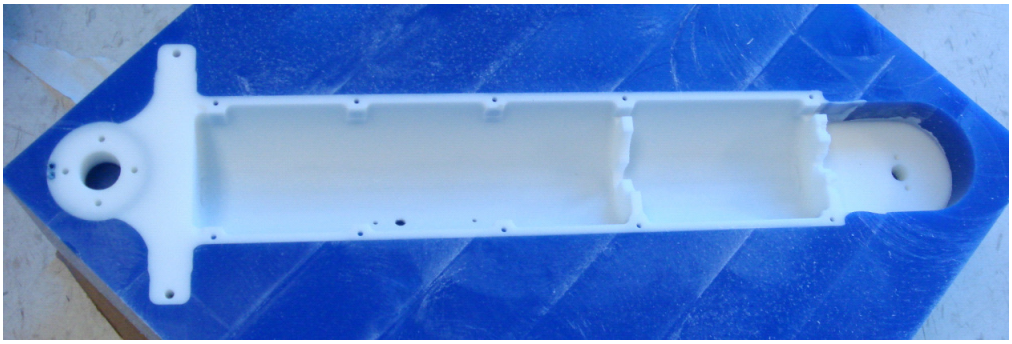

Figure 6: Complete Half Structure of Upper Arm Before Removing Wax Mold

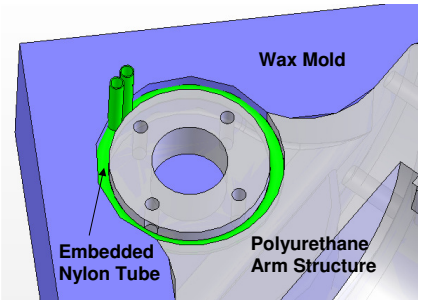

(a) SDM Process for Embedding Nylon Tube

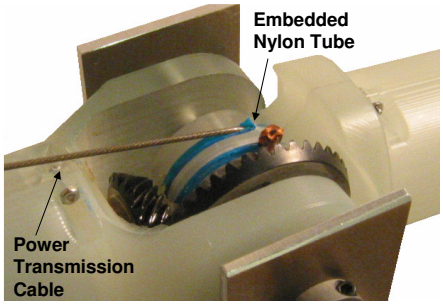

(b) Embedded Nylon Tube for Cable

Figure 7: To create a conduit for the cable that is pulled by the Mckibben actuators, a hollow nylon tube was embedded in the pulley, and part of it was removed.

9, Shore 85D polyurethane) that houses the valves, bearings, mini actuator, controllers and wiring. Because SDM involves material removal as well as deposition, the dimensional tolerances (typically $\pm$0.05mm) and surface finishes are the same as those obtained with conventional CNC machined parts. The process for fabricating one half of an upper arm link is shown in Fig. 5, and a complete prototype is shown in Fig. 6. Inner components can be embedded

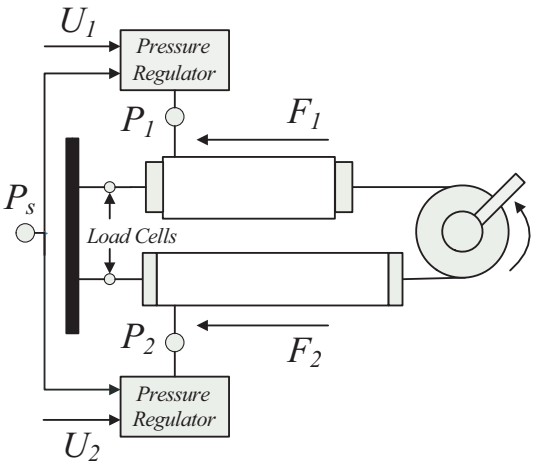

(a) Macro Actuation Schematic

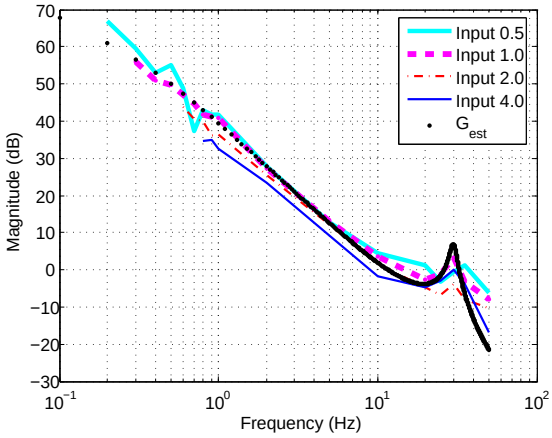

(b) System Identification of Macro Actuation

Figure 8: (a) The macro actuation system includes the pressure regulator and muscles. $P_1(P_2)$, $U_1(U_2)$, $F_1(F_2)$ and P_s denote regulated muscle pressures, command signal, muscle forces, and supply pressure, respectively. (b) Bode plot of the estimated macro actuation system. The results indicate that equations (3) and (4) are good approximations for the system input voltage between 0.5 V and 3 V. For an input of 4 V, the system deviates from the predicted Bode plot due to saturation of the pressure regulator.

during intermediate machining and pouring steps. To create a conduit for the cable that is pulled by the Mckibben actuators, a hollow nylon tube was embedded in the pulley, and part of it was removed as shown in Fig. 7.

3 Control Strategy

The $S2\rho$ robotic arm is controlled employing macro and mini actuators in parallel. The controller partitions the reference input torque between the low frequency macro actuator and the high frequency mini actuator. Because of slow dynamics of the low frequency actuator, the high frequency components of the reference input are directly commanded into the high frequency actuator as the error (Fig. 11 (b)). For low frequency actuation, low impedance output is achieved by using the light and compliant pneumatic muscles connected directly to the joint. For high frequency actuation, low impedance is achieved by using a small, low-inertia motor connected through a low-ratio transmission. This combination reduces the effective inertia of the arm and increases the bandwidth for closed-loop control. However, the original $S2\rho$ 1.0 prototype showed limited performance resulting from the slow dynamics of the macro actuation, which could not be overcome entirely by the mini actuator. The electric actuator tended to saturate, resulting in a temporary degradation of performance and stability. Furthermore, the limited stroke of the pneumatic muscles restricted the range of motion. To address these problems, the new version 1.5 prototype employs four muscles (two each for flexion and extension) which, along with the proportional valves, provide a better combination of power-to-weight ratio, response time, and control accuracy.

3.1 Macro Actuation

A schematic diagram of the antagonistic actuator configuration is shown in Fig. 8 (a) [Sardellitti et al. (2007)]. When a desired torque is to be produced at the joint, the necessary force difference is symmetrically distributed and then compensated using force feedback through load cell measurements, as shown in Fig. 11 (a). The force feedback compensates for the pneumatic muscle force/displacement hysteresis phenomenon while also increasing the actuation bandwidth [Sardellitti et al. (2007)].

In order to design the controller, system identification was first conducted to identify the dynamic behavior of the pneumatic muscles and proportional valves. The proportional valve operates based on the balance between the magnetic force and mechanical force on the spool; when the magnetic force overcomes the pressure, the valve opens. However, since the mechanical force increases as pressure across the valve rises, an experiment was conducted to identify the threshold voltage to open the valve as a function of the muscle pressure. With respect to the pressure of the muscle, P, the threshold voltages, V_{th_p} and V_{th_e}, for pressurizing valves and exhausting valves, respectively can

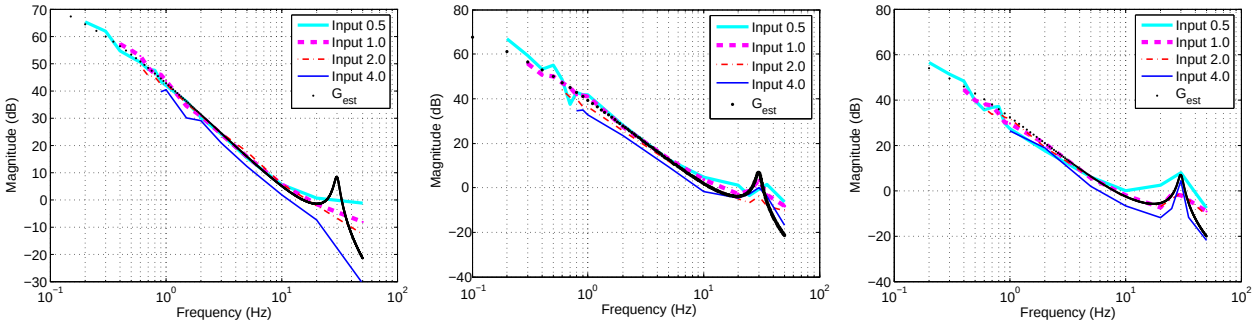

(a) Configuration1 (b) Configuration2 (c) Configuration3

Figure 9: System identification at various joint configurations. The order of the macro actuation system, G_{macro}, is maintained while the system gain changes. The gains with respect to the joint configurations are fit with a cubic spline, which gives $q = -18.34^o$, 1.94^o, and 29.80^o for configuration 1, 2 and 3, respectively.

be approximated with linear equations as

$$V_{th_p} = -0.013 \times P + 2.376 \quad : \text{Pressurizing Valve} \tag{1}$$
$$V_{th_e} = 0.031 \times P + 1.320 \quad : \text{Exhausting Valve} \tag{2}$$

Since the mechanical force of the valve is provided by a spring-damper system, the dynamics between the input voltage, U, and flow rate, Q, can be approximated for low frequencies using an integrator with second order dynamics [Kontz (2007)]. The pneumatic muscles can be approximated by a first order system, determined experimentally [Sardellitti et al. (2007)]. Thus, the transfer function of the entire macro actuation system, G_{macro}, which is the merged system of valves and muscles, is given by

$$\begin{aligned} G_{macro} \quad = G_{valve} \cdot G_{muscle} \quad &= \frac{X}{U}\frac{Q}{X} \cdot \frac{P}{Q}\frac{F}{P} \\ &= K_{valve} \frac{s + z_{valve}}{s(s^2 + 2\zeta\omega s + \omega^2)} \cdot K_{muscle} \frac{s + z_{muscle}}{\tau s + 1} \end{aligned} \tag{3}$$

where, X, P, F, K_{valve}, and K_{muscle} are valve spool position, muscle pressure, muscle force, system gain of the valve, and system gain of the muscle, respectively. z_{valve} and z_{muscle} are the zeros of the valve and the muscle, respectively, which are obtained experimentally.

To identify the macro actuation system as shown in Fig. 8 (a), sinusoidal inputs with various frequencies were used. Although the system includes manifold and tube dynamics, which are hard to measure, the experimental results indicate that equations (3) are a good approximation for the system for inputs between 0.5 V and 3 V. However, as seen in Fig. 8 (b), for an input of 4 V, the curve deviates from the prediction due to saturation of the pressure regulator. The lumped parameter values at joint angle of 1.94^o are given in Table 2.

$K = K_{valve} \cdot K_{muscle}$	100	τ	2.5
ζ	0.1	ω	28
z_{muscle}	20	z_{valve}	30

Table 2: Lumped Parameters of Macro Actuation System ($q = 1.94^o$)

Experiments with respect to different configurations, which are associated with joint angles, demonstrate that muscle dynamics depend on muscle length. Fig. 9 shows the same system order is maintained while the system gain changes. ($q = -18.34^o$, 1.94^o, and 29.80^o for three typical configurations) With seven different configurations between -42.21^o and 37.10^o, we conclude that the system gain with respect to the joint angle can be fit adequately with a cubic spline:

$$K = -4.2 \times 10^{-4} q^3 + 7.4 \times 10^{-3} q^2 + 1.5q + 97 \tag{4}$$

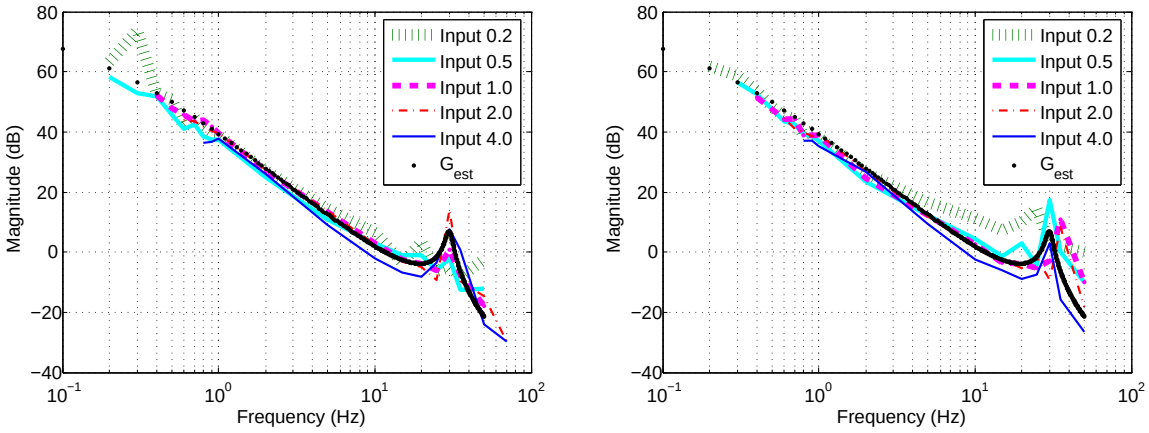

(a) Configuration2 at 110.32 KPa

(b) Configuration2 at 275.79 KPa

(c) Configuration3 at 110.32 KPa

(d) Configuration3 at 275.79 KPa

Figure 10: System identification with various initial pressures. Fig. (a) and (c) shows the actual system is well matched by the estimated system when the pneumatic muscle initially contains air at low pressure of 110.32 KPa (16 psi). However, at higher initial pressure of 275.79 KPa (40 psi), the actual system differs from the estimated system, especially with a small input at high frequency as shown in Fig. (b) and (d).

A non-linear effect is observed for low amplitude input commands. Fig. 10 (a) and (c) shows that the actual system is well matched by the estimated system, even at high frequency, when the pneumatic muscle initially contains air at low pressure. However, some deviation from the estimated system is observed with an input of 4.0 V, which causes valve saturation. At higher initial pressure, the actual system is less well approximated by the estimated system, especially with small inputs at high frequency as shown in Fig. 10(b) and (d). These results are expected, as the pressure regulator flow rate is governed by the equation,

$$Q = CX\sqrt{\Delta P} \tag{5}$$

where Q, C, X, and ΔP are the flow rate of pressure regulator, the flow constant, the plunger/spool position, and the pressure difference across the regulator, respectively [Kontz (2007)]. At higher pressures, the pressure difference seems to dominate the flow rate rather than the small plunger/spool displacement corresponding to small input command. Furthermore, the response of the plunger/spool is limited at high frequency. In the next section, we discuss how we accommodate this nonlinear effect in the hybrid control strategy.

Among the tested compensators, based on the previously described system identification, a PID controller provides the best performance. A PI controller has good tracking performance, but significant phase delay at high frequency and a PD controller has significant tracking errors. Fig. 11 (a) demonstrates that the compensator gain of the macro force control is adapted with respect to the configuration, which is associated with the lengths of the pneumatic muscles.

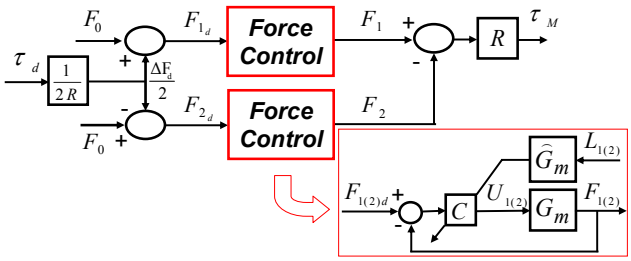

(a) Macro torque control with adaptive force control

(b) Hybrid Actuation

Figure 11: (a) The Force Control block represents the adaptive force controller of an individual muscle. This demonstrates that the compensator gain of macro force control is adapted with respect to the configuration, i.e., the pneumatic muscles length. R and L denote the radius of the pulley and the length of muscle, respectively. (b) The torque applied on the joint will then be the linear combination of the macro and mini torque contributions. Mechanical advantages such as low gear reduction ratio and near-collocated actuator allow us to assume that desired torque is achieved at the joint. The faster dynamics of the mini actuator compensate for the slow dynamics of the pneumatic muscle.

The PID controller with adaptive gain in frequency domain is given by

$$C = \frac{22.5}{K}\frac{s+6}{s+300}\frac{s+25}{s+0.01} \tag{6}$$

where, K is given by equation 4.

Chou developed the analytical model of the pneumatic muscle as

$$F = \frac{Pb^2}{4\pi n}\left(\frac{3L^2}{b^2} - 1\right) \tag{7}$$

where, F, P, and L are force, pressure, and length of the muscle, respectively. The terms b and n are muscle constants [Chou and Hannaford (1996)]. Although this model has been widely used in a number of robotic arms utilizing pneumatic muscles, the model predicts a different force output from what was measured since the model does not

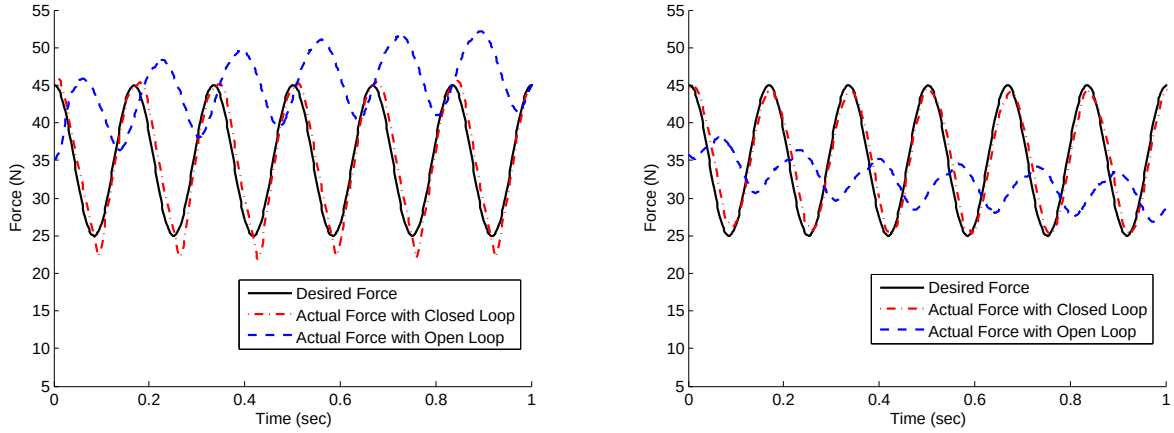

(a) Macro Force Control at Configuration 2

(b) Macro Force Control at Configuration 3

Figure 12: Macro force control comparison for open-loop and closed loop control at 6Hz, the bandwidth of the macro closed loop force control. Closed-loop PID control with force feedback through a load cell significantly improves force control performance over the open-loop control that uses the pneumatic muscle analytical model alone [Sardellitti et al. (2007)]. Fig. (a) and (b) demonstrate the force feedback PID control tracks the reference input consistently regardless of the muscle length, while the open-loop control shows significant deviation from reference input command and different behavior depending on the muscle length.

account for the non-linearities of pneumatic muscles. Previous efforts to develop an adequate yet simple model include introducing an effectiveness term [Colbrunn et al. (2001)], and modeling friction [Tondu and Lopez (2000); Tondu and Zagal (2006)]. However, the viscous friction and air compressibility produce high non-linearity, which substantially depends on the length of muscles. Furthermore, the difficult measurement of muscle constants raises another possibility of error. These problems consequently result in inconsistent open-loop control performance at different configurations, which are associated with the muscle lengths. The closed loop PID control with force feedback through a load cell significantly compensates high non-linearity and inconsistency while improving force control performance over the open-loop control that uses the pneumatic muscle analytical model alone [Sardellitti et al. (2007)]. As shown in Fig. 12, the closed loop PID control works successfully at 6Hz, the bandwidth of the macro closed loop force control, while the open-loop control shows significant deviation from a reference input command.

3.2 Mini Actuation

The measured torque error of the macro actuation is directly commanded to the mini actuator as shown in Fig. 11 (b). For the mini controller, an open-loop torque controller is implemented. The characteristics of the mini, including a low gear reduction ratio and near-collocated actuator, allow us to assume that the desired torque of the mini actuation is achieved at the joint.

4 Experimental Results

In order to validate the hybrid actuation concept for the human-friendly robot, we built a one-degree-of-freedom testbed as explained in Section 2 and shown in Fig. 2. For performance analysis, open-loop contact force tests and position control tests with hybrid actuation were conducted. For safety analysis, the normalized effective mass was simulated and compared to other robotic arms.

4.1 Performance Characteristics

In order to verify the performance of macro actuation, experiments were conducted comparing the results obtained with a simple P and PID controller. As shown in Fig. 13 (a) and (b), PID shows better performance at high frequency in terms of tracking error and phase delay.

Since the internal load cell measures not final joint torque but pneumatic muscle force, the mini actuator does not affect load cell measurement at a fixed configuration. Therefore, the contact force at the end-effector is measured with an external force sensor to verify the contribution of the mini actuator in achieving force control at a given configuration. Fig. 13 (c) and (d) show the performance difference between the macro actuation alone and hybrid actuation. Hybrid actuation achieves a force control bandwidth of 26Hz while macro actuation achieves 6Hz. A negligible steady state error of contact force with hybrid actuation demonstrates that open-loop torque control is satisfactory for the mini actuator.

Experiments of position tracking at increasing frequency were also conducted. A position controller, using feedback from an encoder placed at the mini motor, was implemented as an outer loop wrapped around the inner hybrid actuation controller. Position tracking experiments were conducted for the macro actuation and the hybrid actuation. In Fig. 13 (e) and (f), the position tracking control of the macro alone and the hybrid actuation are plotted for a sinusoidal reference input, of which frequency is 6Hz and amplitude is 5^o. The result shows that the hybrid actuation shows significant performance improvement over the macro actuation alone in compensating for the non-linear effect of the pneumatic muscles. In addition, the results demonstrate that the new design and control scheme of $S2\rho$ overcomes the performance limitations of the $S2\rho$ 1.0, for which the position control bandwidth was 2Hz [Shin et al. (2008)].

4.2 Increasing Safety Characteristics with Reduced Inertia

Since safety is a primary requirement for human-friendly robots, it is desirable to establish quantitative criteria for making comparisons. Robot safety is a function of impact velocity, interface stiffness between the robot and human, and effective inertia [Zinn (2005)]. The impact velocity depends on maximum joint velocity, which is intrinsically bounded by actuator dynamic specifications. The compliance and damping of the robot skin are also critically important design parameters, but beyond the scope of this paper. For a given impact velocity and angle, the remaining critical parameter is the effective inertia, which can be graphically illustrated as a belted ellipsoid over the workspace plane [Khatib (1995)]. Fig. 14 (b) and (c) display the effective mass at the same shoulder and elbow configurations of $q_1 = 20^o$ and $q_2 = -90^o$ (Fig. 14) for a PUMA560, the DM^2, human and the S2ρ 1.5. The diagram demonstrates that the effective hybrid actuation approach reduces the effective mass by approximately a factor of three compared to the previous DM^2. The S2ρ 1.5 has a maximum effective mass of 0.98kg as compared to 3.51kg for DM^2, while a conventional robot such as PUMA560 has the far greater effective mass of 24.88kg.

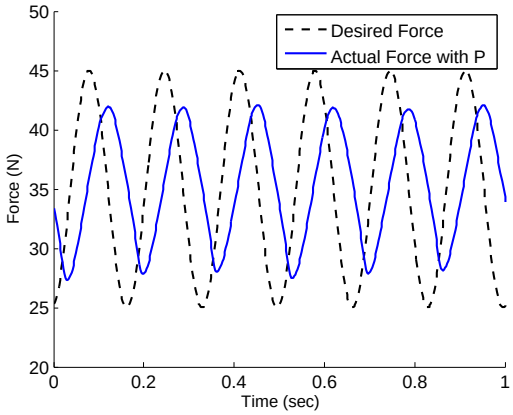

(a) Macro Force Control with a P controller

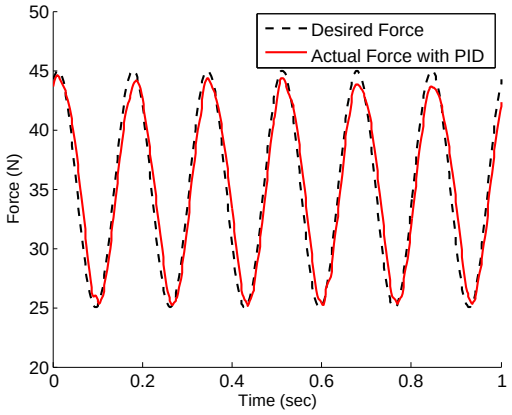

(b) Macro Force Control with a PID controller

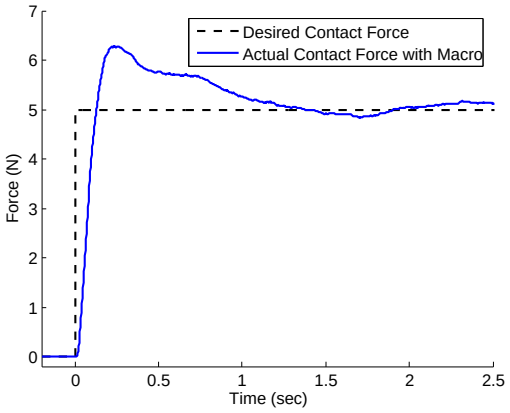

(c) Contact Force Control with Macro Actuation

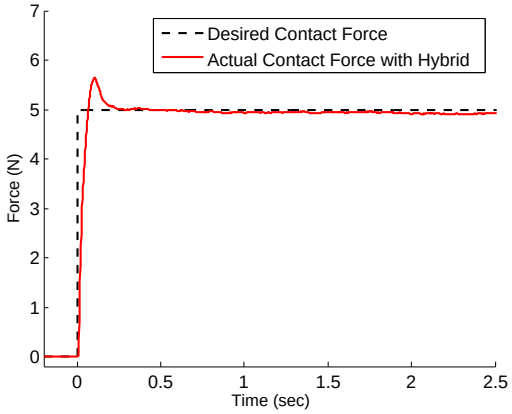

(d) Contact Force Control with Hybrid Actuation

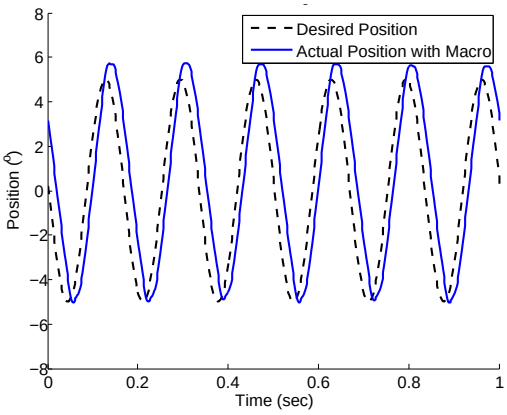

(e) Position Control with Macro Actuation

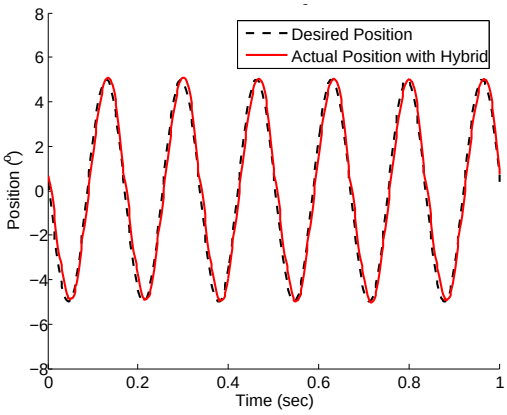

(f) Position Control with Hybrid Actuation

Figure 13: (a) and (b): Force control comparison for P and PID controllers at 6Hz. PID shows better performance at higher frequency in tracking error and phase delay. (c) and (d): Open-loop contact force control comparison for macro and hybrid control. Hybrid actuation achieves a bandwidth of 26Hz while macro actuation achieves 6Hz. (e) and (f): Position tracking control comparison for macro and hybrid control with a sinusoidal reference input ($\pm$ 5^o at 6Hz). Hybrid actuation shows significant improvement over the system with macro actuation alone.

However, a lower effective mass may come at the expense of reduced performance if the lower effective mass is a consequence of using lower gear ratios and smaller actuators. Therefore, the safety analysis needs to incorporate additional constraints that enable comparisons among manipulators at the same level of performance. As shown in Fig. 14 (d), the effective mass of each robotic arm is normalized by its own payload, so that the safety comparison between robotic arms with different size/payload can be made. While the PUMA560 and DM^2 have normalized effective masses of 1.15 and 0.058, S2ρ shows only 0.032. The improved result compared to the previous DM^2 approach shows that the safety of S2ρ is not compromised by the addition of large muscles. For an additional comparison, we provide the normalized effective mass of an average U.S. male civilian arm, which is sampled from surveys of U.S. populations [Chaffin et al. (2006); NASA (1995)] and assuming a working payload of approximately 62 N for repeated manipulations.

5 Conclusion and Future Work

The concept of hybrid actuation is presented with a revised version of the Stanford Safety Robot Arm, S2ρ. Four pneumatic muscles connected in an antagonist configuration provide a wider range of motion than a two-muscle design, with improved joint torque and responsiveness. New pressure regulators with proportional valves also improve the response time in transient conditions and reduce steady state errors. A rapid prototyping method, Shape Deposition Manufacturing, enables the integration of power sources as well as mechanical components in a single structure so that the system can be lighter, stronger and more compact. A PID force feedback control with load cells improves the performance of macro actuation and confirms the results of system identification for various muscle conditions. With the inclusion of open-loop torque control for the mini actuator, the hybrid system shows significant performance improvement over the arm with pneumatic actuation alone. Simulations using the normalized effective mass/inertia validate the arm safety characteristics, which are comparable to those of a human arm.

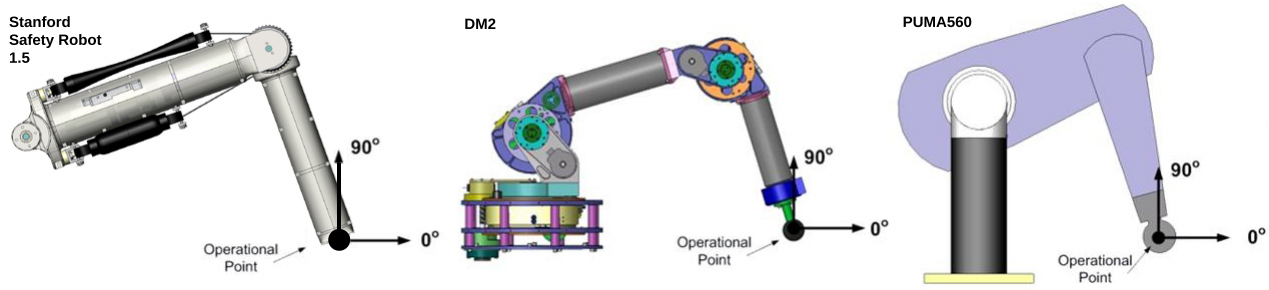

(a) Configurations for Effective Mass Calculation

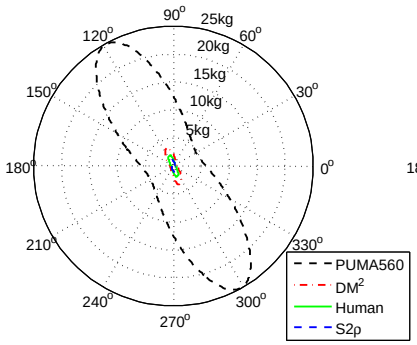

(b) Effective Mass

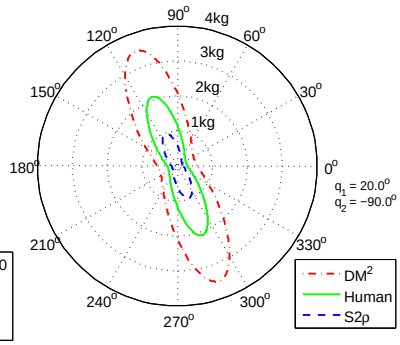

(c) Effective Mass(Zoomed-In)

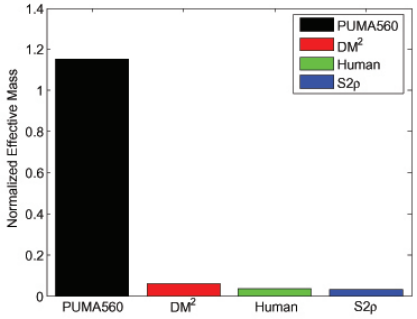

(d) Normalized Effective Mass

Figure 14: (a) Effective masses of each robotic arms are calculated at $q_1 = 20^o$ and $q_2 = -90^o$. (b) and (c) Effective mass of PUMA560, DM^2, S2ρ and Human. S2ρ has a maximum effective mass of 0.98kg as compared to 3.51kg for DM^2 and 2.11kg for the Human, while the conventional PUMA560 has an effective mass of 24.88kg. (d) Normalized effective Inertia. Effective inertia is normalized by payload for better comparison. The PUMA560 has a normalized effective mass of 1.15 but S2ρ shows only 0.032.

As with human muscle, a larger cross section and larger number of pneumatic actuators provide higher joint torques. However, higher joint torque and a wide range of motion are competing objectives with respect to a pulley radius. To achieve a desired combination of joint torque and range of motion for a particular application we can vary the number and size of the muscles and the pulley radius, which can also vary with angle. Further design studies will concern the sizing of the mini actuator and the selection of its transmission ratio. As the macro controller becomes more responsive, the demands on the mini actuator reduce, which provides further opportunities for weight reduction.

Additional improvements are possible in the choice of materials. Fiber reinforcement of the main SDM structure will provide a higher specific stiffness and strength. The development of a compliant outer skin with tactile sensors is another area of ongoing work. The skin will help to absorb impact energy and, if equipped with proximity sensors, warn of impending collisions. In addition, the skin will contain the effects of a rupture if one of the muscles should burst under pressure. Even so, there is the the potential for high transient torques in the event of a muscle failure; therefore we are also planning to add a brake at each joint.

Acknowledgements

The authors gratefully acknowledge the support of General Motors. In addition, the authors recognize the contributions of Marc Strauss at Artificial Intelligence Laboratory, Stanford University and Fabian Seitz at Autonomous Systems Laboratory, ETH.

Appendix: Index to Multimedia Extensions

The multimedia extension page is found at http://www.ijrr.org

Extension	Type	Description
1	Video	Force control with gravity compensation
2	Video	Disturbance rejection comparison between macro actuation alone and hybrid actuation

References

Bicchi, A., Peshkin, M., and Colgate, J. E. 2008. Safety for physical human-robot interaction. *Springer Handbook of Robotics 2008*, pages 1335–1348.

Bicchi, A. and Tonietti, G. 2004. Fast and soft arm tactics: Dealing with the safety-performance trade-off in robot arms design and control. *IEEE Robotics and Automation Magazine*, 11:22–33.

Caldwell, D. G., Medrano-Cerda, G. A., and Goodwin, M. J. 1995. Control of pneumatic muscle actuators. *IEEE Control Systems Magazine*, 15(1)(1):40–48.

Chaffin, D., Andersson, G., and Martin, B. 2006. Occupational biomechanics. *Fourth Edition, Wiley*, 2:47–49.

Cham, J. G., Bailey, S. E., Clark, J. C., Full, R. J., and Cutkosky, M. R. 2002. Fast and robust: Hexapedal robots via shape deposition manufacturing. *International Journal of Robotics Research*, 21(10-11):869–882.

Chou, C. P. and Hannaford, B. 1996. Measurement and modeling of mckibben pneumatic artificial muscles. *IEEE Robotics and Automation Magazine*, 12(1):90–102.

Colbrunn, R. W., Nelson, G. M., and Quinn, R. D. 2001. Modeling of braided pneumatic actuators for robotic control. *Proceedings of the 2001 IEEE/RSJ International Conference on Intelligent Robots and Systems*, 4:1964–1970.

De Luca, A., Albu-Schaffer, A., Haddadin, S., and Hirzinger, G. 2006. Collision detection and safe reaction with the dlr-iii lightweight manipulator arm. *Proc. Intelligent Robots and Systems*, pages 1623–1630.

Ebert, D. M. and Henrich, D. D. 2002. Safe human-robot-cooperation: Image based collision detection for industrial robots. *Proc. IEEE/RSJ Int. Conf. on Intelligent Robots and Systems*, pages 1826–1831.

English, C. and Russell, D. 1999. Mechanics and stiffness limitations of variable stiffness actuator for use in prosthetic limbs. *Mechanism and machine theory*, 34(1).

Haddadin, S., Albu Schaffer, A., and Hirzinger, G. 2007. Safety evaluation of physical human-robot interaction via crash testing. *Robotics: Science and Systems Conference*.

Haddadin, S., Albu Schaffer, A., and Hirzinger, G. 2008. The role of the robot mass and velocity in physical human-robot interaction - part i: Unconstrained blunt impacts. *IEEE Int. Conf. on Robotics and Automation, Pasadena, USA, 2008*, pages 1331–1338.

Heinzmann, J. and Zelinsky, A. 2003. Quantitative safety guarantees for physical human-robot interaction. *Int. J. of Robotics Research*, 22(7-8):479–504.

Khatib, O. 1986. Real time obstacle avoidance for manipulators and mobile robots. *International Journal of Robotics Research*, 5(1):90– 99.

Khatib, O. 1995. Inertial properties in robotic manipulation: An object-level framework. *International Journal of Robotics Research*, 14(1):19–36.

Kontz, M. 2007. Haptic control of hydraulic machinery using proportional valves. *PhD thesis, Georgia Institute of Technology, Atlanta, GA*.

Lumelsky, V. and Cheung, E. 1993. Real-time collision avoidance in teleoperated whole-sensitive robot arm manipulator. *IEEE Trans. on Systems, Man, and Cybernetics*, 23(1):194–203.

Migliore, S. A., Brown, E. A., and DeWeerth, S. P. 2005. Biologically inspired joint stiffness control. *IEEE International Conference on Robotics and Automation*, pages 4508–4513.

Morrel, J. B. 1996. Parallel coupled micro-macro actuators. *PhD thesis, Massachusetts Institute of Technology, Cambridge, MA*.

NASA 1995. Man-systems integration standards. *NASA-STD-3000*, 1:Section 4.

Novak, J. L. and Feddema, I. T. 1992. A capacitance-based proximity sensor for whole arm obstacleavoidance. *Proc. of the 1992 IEEE International Conference on Robotics and Automation*, 2:1307–1314.

Pratt, G. and Williamson, M. 1995. Series elastic actuators. *Proc. of the 1995 IEEE/RSJ International Conference on Intelligent Robots and Systems*, 1:399–406.

Salisbury, J. K., Eberman, B. S., Townsend, W. T., and Levin, M. D. 1989. Design and control of an experimental whole-arm manipulator. *Proc. of the 1989 International Symposium on Robotics Research*.

Sardellitti, I., Park, J., Shin, D., and Khatib, O. 2007. Air muscle controller design in the distributed macro-mini(dm^2) actuation approach. *Proc. of the 2007 IEEE/RSJ International Conf. on Intelligent Robots and Systems*.

Schiavi, R., Grioli, G., Sen, S., and Bicchi, A. 2008. Vsa–ii: A novel prototype of variable stiffness actuator for safe and performing robots interacting with humans. *IEEE International Conference on Robotics and Automation*.

Shin, D., Sardellitti, I., and Khatib, O. 2008. A hybrid actuation approach for human-friendly robot design. *Proc. of the 2008 IEEE International Conference on Robotics and Automation*.

Thaulad, P. 2005. Human friendly robot control system design and experimental validation. *Degree of Engineer Thesis, Stanford University, Stanford, CA*.

Tondu, B. and Lopez, P. 2000. Modeling and control of mckibben artificial muscle robot actuators. *IEEE Control Systems Magazine*, 30:15–38.

Tondu, B. and Zagal, S. D. 2006. Mickebben artificial muscle can be adapted to be in accordance with the hill skeletal muscle model. *IEEE Internation Conference on Biomedical Robotics and Biomechatronics*.

Tonietti, G. and Bicchi, A. 2002. Adaptive simultaneous position and stiffness control for a soft robot arm. *IEEE/RSJ International Conference on Intelligent Robots and Systems*, pages 1992–1997.

Van Ham, R., Vanderborght, B., Van Damme, M., Verrelst, B., and Lefeber, D. 2007. Maccepa, the mechanically adjustable compliance and controllable equilibrium position actuator: Design and implementation in a biped robot. *Robotics and Autonomous Systems*, 55(10):761–768.

Van Ham, R., Verrelst, B., Daerden, F., and Lefeber, D. October 2003. Pressure control with on-off valves of pleated pneumatic artificial muscles in a modular one-dimensional rotational joint. *International Conference on Humanoid Robots*, page 35.

Weiss, L. E., Merz, R., Prinz, F. B., Neplotnik, G., Padmanabhan, P., Schultz, L., and Ramaswami, K. 1997. Shape deposition manufacturing of heterogeneous structures. *Journal Of Manufacturing Systems*, 16(4):239–248.

Wolf, S. and Hirzinger, G. 2008. A new variable stiffness design: matching requirements of the next robot generation. *IEEE Inter. Conf. Robotics and Automation*.

Zinn, M. 2005. A new actuation approach for human friendly robotic manipulation. *PhD thesis, Stanford University, Stanford, CA*.

Zinn, M., Roth, B., Khatib, O., and Salisbury, J. K. 2004. New actuation approach for human-friendly robot design. *International Journal of Robotics Research*, 23(1):379–398.